



RESEARCH ARTICLE

# Optimal design of a generalized single-loop parallel manipulator with RCM characteristic considering motion/force transmissibility

Luquan Li<sup>1</sup> , Chunxu Tian<sup>1</sup>, Zhihao Xia<sup>1</sup> and Dan Zhang<sup>2</sup> 

<sup>1</sup>Institute of AI and Robotics, Academy for Engineering & Technology, Fudan University, Shanghai, PR China

<sup>2</sup>Department of Mechanical Engineering, The Hong Kong Polytechnic University, Hung Hom, Kowloon, Hong Kong

**Corresponding author:** Dan Zhang; Email: [dan.zhang@polyu.edu.hk](mailto:dan.zhang@polyu.edu.hk)

**Received:** 23 May 2024; **Revised:** 27 November 2024; **Accepted:** 22 December 2024; **First published online:** 21 January 2025

**Keywords:** generalized single-loop parallel manipulator; RCM; reconfigurable base; motion/force transmissibility

## Abstract

In certain scenarios, the large footprint of a robot is not conducive to multi-robot cooperative operations. This paper presents a generalized single-loop parallel manipulator with remote center of motion (GSLPM-RCM), which addresses this issue by incorporating a reconfigurable base. The footprint of this RCM manipulator can be adjusted by varying the parameters of the reconfigurable base. First, utilizing configuration evolution, a reconfigurable base is constructed based on the principle of forming RCM motion. Then, according to the modular analysis method, the inverse kinematics of this parallel RCM manipulator is analyzed, and the workspace is also analyzed. Subsequently, the motion/force transmissibility of this RCM manipulator is analyzed by considering its single-loop and multi-degree of freedom characteristics. Leveraging the workspace index and transmissibility indices, dimension optimization of the manipulator is implemented. Finally, the influence of the reconfigurable base on the workspace and the transmissibility performance of the optimized manipulator is studied.

## 1. Introduction

In minimally invasive surgery (MIS), surgeons insert surgical tools into the patient's body through a small external incision and perform operations directly outside the body [1]. MIS offers benefits such as reduced surgical incisions and shorter recovery times, but it also demands a higher level of skill from the surgeon [2]. In comparison, robotic-assisted MIS provides greater accuracy, safety, and stability, assisting doctors in performing surgical procedures more effectively. Within robotic-assisted MIS, the RCM mechanism serves as an execution device, and its output link can move around a distal stationary point without physical joint constraints.

In recent years, various RCM mechanisms with different degrees of freedom (1-DOF [3], 2-DOF [4–12], 3-DOF [13–24], and 4-DOF [25–31]) are developed. Among them, the 4-DOF RCM mechanism stands out due to its ability to generate three rotational and one translational motion. As a result, it can implement complex surgical operations and is widely applied to laparoscopic surgery. In comparison, full parallel mechanisms offer advantages in terms of precision, stiffness, payload, kinematics, and dynamics over serial and hybrid counterparts, especially in terms of precision. For example, Kong and Gosselin studied the structure synthesis of SP-equivalent parallel manipulators (PMs) with RCM characteristics [30]. Li et al. [32] proposed a special family of 4-DOF RCM PMs with four limbs, each driven by a fixed linear actuator. Zoppi et al. [33] studied a 4-DOF RCM parallel mechanism with four identical 5R legs (R: joint). The RCM point of these mechanisms is situated within the mechanism,

with the limbs arranged around it. However, this internal placement of the mechanism could lead to a substantial footprint, potentially hindering effective multi-robot collaboration. Furthermore, due to the multi-limb and multi-closed-loop structures, most full parallel mechanisms exhibit certain limitations, such as complex structure and kinematic analysis, limited workspace, and internal singularities. To circumvent these challenges, researchers have introduced several single-loop RCM parallel mechanisms. Qiu et al. [28] presented a 4-DOF RCM parallel surgical robot with two limbs based on a parallelogram mechanism. Chen et al. [34] developed a spatial  $3R1T$  ( $R$ : rotation;  $T$ : translation) RCM PM with two 2-URRH limbs. Li et al. [13] synthesized a class of GSLPMs-RCM with a multi-DOF drive unit. To meet the diverse demands of surgical procedures, researchers have developed some RCM mechanisms with reconfigurable characteristics. Wang et al. [35] proposed an RCM parallel mechanism with metamorphic characteristics using the parallelogram joint. Liu et al. [36] introduced a four-limbed reconfigurable PM, capable of switching between motion modes:  $1R1T$ ,  $2R1T$ , and  $3R1T$ . Additionally, Essomba et al. [37] introduced a spherical PM with a reconfigurable base for robotic-assisted craniotomy, analyzing the influence of reconfigurable parameters on workspace and kinematic performances. Essomba and Wang [38] proposed an RCM mechanism with controllable center of rotation using a spherical reconfiguration linkage.

Beyond the structural design of RCM mechanisms, their kinematic performance also receives special attention. Generally, the condition number [39], dexterity [28], manipulability [40], and motion/force transmission [19] are used to evaluate the kinematic performance of RCM parallel mechanisms. When dealing with mechanisms possessing both translational and rotational DOFs, indices based on the Jacobian matrix encounter challenges due to non-homogeneous units [33], resulting in unclear physical interpretations. Consequently, the reliability of performance assessment is compromised. The motion/force transmission index is a scale-free indicator that is not affected by coordinate systems [41]. Various approaches and indices, predicated on motion/force transmission, are studied to analyze the performance of parallel mechanisms featuring diverse structural configurations. For example, a generalized transmission index was introduced by Chen et al. [42] to evaluate the performance of spatial mechanisms. Liu et al. [43] introduced a method for singularity analysis of parallel manipulators by considering motion/force transmissibility. Chen et al. [44] assessed the transmissibility of a six-limbed 5-DOF parallel machining robot by employing the mean of the minimum virtual power transmissibility. Li et al. [45] proposed new transmission indices for redundantly actuated PMs. Additionally, Meng et al. [46] introduced an evaluation approach to analyze the motion-force interaction performance of the PMs featuring closed-loop passive limbs.

This paper presents a novel GSLPM-RCM featuring a reconfigurable base that utilizes a parallelogram linkage. Utilizing its reconfiguration capability, the RCM mechanism can adjust the footprint and workspace layout to accommodate a variety of operational demands. The structure of this paper is as follows: Section 2 details the design process for the GSLPM-RCM with a reconfigurable base. Section 3 analyzes the kinematics and workspace of the GSLPM-RCM. Section 4 analyzed the transmission indices for the GSLPM-RCM. Section 5 implements dimension optimization using the strength Pareto evolutionary algorithm II (SPEA-II) and investigates the impact of the reconfigurable base on the workspace and transmissibility performance. Finally, the paper is summarized in Section 6.

## 2. Structure design

### 2.1. Reconfigurable base

A GSLPM-RCM is presented based on the spherical surface geometric model introduced in previous work [13], as depicted in Figure 1(a). This mechanism consists of a fixed rigid base, two  $R[\text{Pa}]^{\text{III}}R$  limbs, and a specific connecting structure (SCS), wherein a double parallelogram linkage constitutes a  $[\text{Pa}]^{\text{II}}$  joint. To accommodate diverse task requirements, the mechanism features a reconfigurable base designed to adjust its parameters, thereby adjusting the mechanism's characteristics to fit different needs. The occupied space of the mechanism can be changed through its reconfigurable base, while also

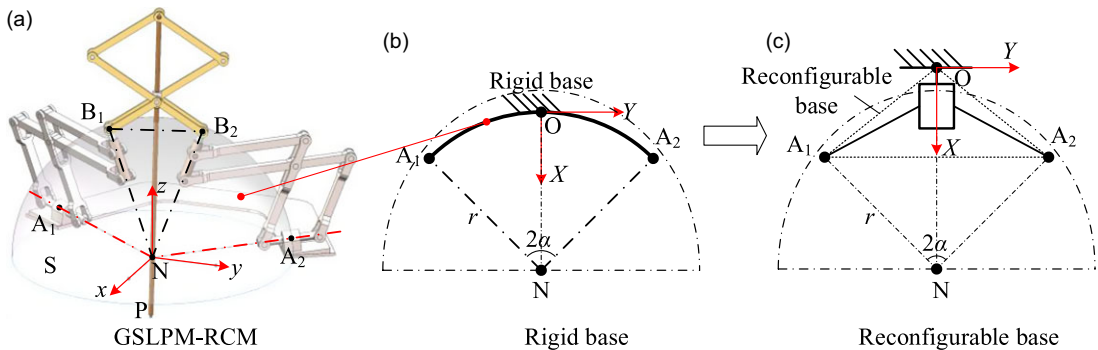


**Figure 1.** The concept of the mechanism with a reconfigurable base.

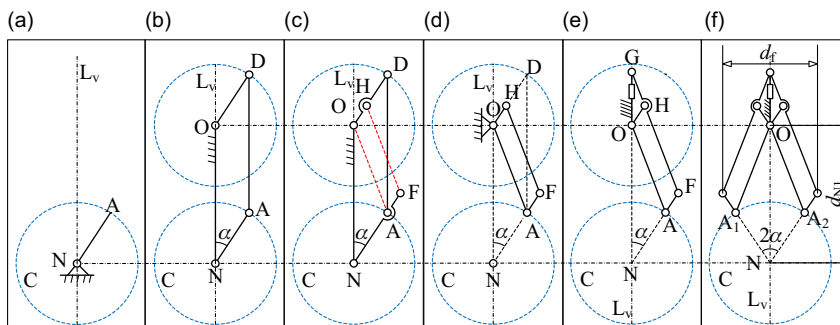


**Figure 2.** The evolution process of the reconfigurable base linkage.

allowing for adjustments in key performance aspects, including workspace shape and operating posture range. These adjustments enable the mechanism to adapt to various operational scenarios and to execute a range of tasks effectively. A key challenge in the design of a reconfigurable base lies in ensuring it meets the necessary constraints to facilitate coordinated movement between the limbs. Specifically, the rigid base is depicted as the circular arc  $A_1A_2$  in Figure 1(b), characterized by a radius of  $r$  and a central angle of  $2\alpha$ . The base determines three key parameters: the radius  $r$ , the central angle  $2\alpha$ , and the position of the RCM point  $N$  ( $x_N, y_N, z_N$ ). Since the endpoint  $B_i$  of the limb  $A_iB_i$  always moves on a spherical surface  $S$ , the reconfigurable base needs to ensure that the first axis  $a_i$  of limb- $i$  always passes through the RCM point  $N$ , while point  $A_i$  remains on a virtual circle with the same fixed radius  $r$ . A concept diagram of the reconfigurable base is established as depicted in Figure 1(c), where the central angle  $2\alpha$  and the position  $N$  ( $x_N, y_N, z_N$ ) serve as variable parameters.

Then, the configuration evaluation process of a reconfigurable base is described as follows:

**Step 1:** Construct a 1-DOF linkage with a link and a R joint as shown in Figure 2(a). The link  $NA$  rotates around point  $N$ , while its endpoint  $A$  is constrained to move along circle  $C$  with a constant radius  $r$ . There is a physical R joint at the center point  $N$  to constrain the link  $NA$ .

**Step 2:** Construct a parallelogram linkage  $ONAD$ , as shown in Figure 2(b). As a result, the actuated R joint at point  $N$ , shown in Figure 2(a), can be moved to point  $O$ . To obtain a virtual center point  $N$  of the circle  $C$ , the link  $ON$  and  $NA$  need to be removed.

**Step 3:** Extend the link  $NA$  to point  $F$  as shown in Figure 2(c). Then construct a virtual parallelogram linkage  $OAFH$ , where the length of  $OA$  is variable. The parallelogram linkage  $ONAD$  constrains the motion of the virtual parallelogram linkage  $OAFH$ .

**Step 4:** Keep the length of link  $OA$  constant and then construct a parallelogram linkage  $OAFH$ , as shown in Figure 2(d). It is essential that the parallelogram linkage  $OAFH$  is constrained by the virtual

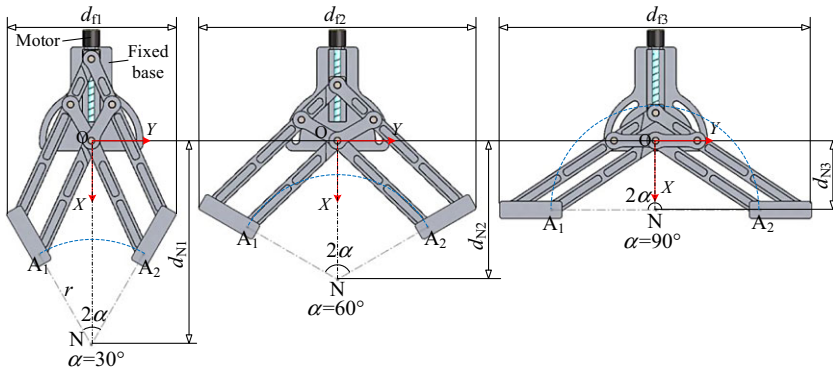


**Figure 3.** The configurations of the reconfigurable base with different central angle  $2\alpha$ .

parallelogram linkage ONAD. This constraint ensures that point A consistently resides on circle C with a fixed radius  $r$ . The length of ON is variable, while the length of NA is fixed and equal to  $r$ . The center point N can move along line  $L_v$ . Although the links ON and NA are removed, a virtual constraint still exists.

**Step 5:** Extend link FH to point G, ensuring that point G is positioned on the line  $L_v$ , as shown in Figure 2(e). By applying the judgment theorem of similar triangles, it is established that  $\triangle NAO$  is always similar to  $\triangle OHG$ . Utilizing the properties of these similar triangles, maintain the length of GH, a segment of link FG, as constant while ensuring that point G remains on the line  $L_v$ . As a result, the length of NA is consistently fixed at  $r$ , and the center point N is always located on the line  $L_v$ . To accomplish this, a prismatic (P) joint is introduced between points O and G, then a crank-slider linkage GOH is constructed to constrain the motion of the parallelogram linkage OAFH. This arrangement eliminates the virtual parallelogram linkage ONAD, as shown in Figure 2(d).

**Step 6:** Construct the symmetric linkage OGHFA along the line  $L_v$  to obtain a reconfigurable base, as shown in Figure 2(f). The maximum width denoted as  $d_f$ , of the reconfigurable base, serves as an indicator of the footprint of the mechanism. The position of the center point N can be characterized by the distance between points O and N denoted as  $d_N$ .

The CAD model of the reconfigurable base is built as depicted in Figure 3, which also displays various configurations with distinct central angles of  $2\alpha$ .

Note that the RCM point N can translate along the X-axis; however, this translation is a parasitic motion. Given that the reconstruction of the mechanism is finalized before the surgical intervention, the RCM point remains stationary during the surgery itself. Consequently, the parasitic motion associated with the RCM point does not interfere with the surgical process. As the central angle  $2\alpha$  increases, the footprint index  $d_f$  correspondingly increases, while the distance  $d_N$  of the center point N decreases.

## 2.2. A GSLPM-RCM with a reconfigurable base

A GSLPM-RCM with a reconfigurable base is constructed, as depicted in Figure 4(a). This 4-DOF mechanism is capable of rotating and translating around point N, classifying it as a 3R1T RCM mechanism. A based frame, denoted as  $\{O\}$ : O-XYZ, is established on the fixed base of the reconfigurable base. To describe the RCM motion, an RCM frame  $\{G\}$ : N-xyz is set at the point N, where the unit directional vectors for the axes are defined as  $\mathbf{u} = [1, 0, 0]^T$  for the x-axis,  $\mathbf{v} = [0, 1, 0]^T$  for the y-axis, and  $\mathbf{w} = [0, 0, 1]^T$  for the z-axis. Additionally, a limb frame  $\{L_i\}$ : N- $x_i y_i z_i$  is built to analyze limb- $i$ , as shown in Figure 4(b), where the  $x_i$ -axis follows  $\mathbf{a}_i$ , and the  $y_i$ -axis is perpendicular to the plane  $P_{li}$ . The unit vectors  $\mathbf{t}_i$  and  $\mathbf{e}_i$  are along the  $y_i$  and  $z_i$ -axis, respectively. Notably,  $\iota$  is the angle between  $\mathbf{a}_i$  and XY-plane, and  $\alpha_i$  is the angle between the projection  $NA_i'$  of  $NA_i$  onto the XY-plane and X-axis. Furthermore, the position vector of endpoint  $B_i$  of the limb- $i$  in  $\{G\}$  is denoted as  $\mathbf{b}_i$ . Define  $\mathbf{b}$  and  $\mathbf{k}$

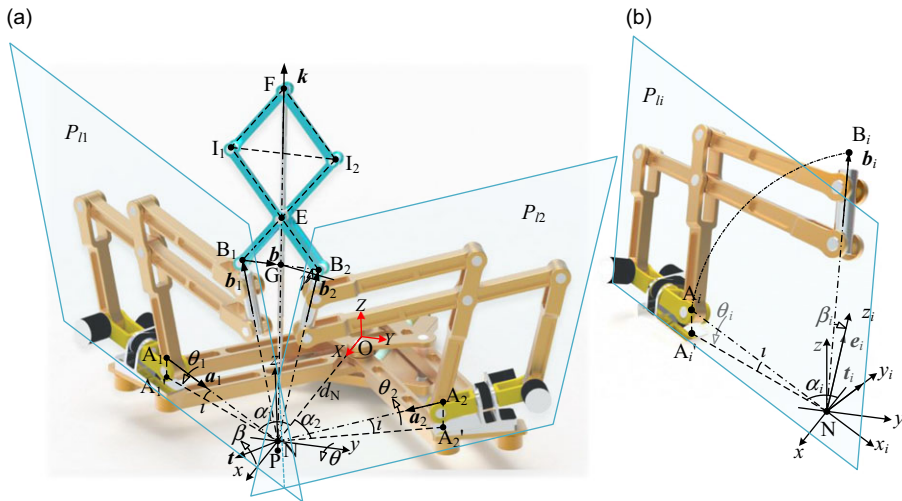


Figure 4. Kinematic diagram of the GSLPM-RCM.

as the unit directional vectors along line  $B_1B_2$  and the output link  $FP$ , respectively.  $\mathbf{P} = [\theta, \beta, \gamma, l_{NP}]^T$  represents the position and orientation of the output link  $FP$ , where  $\theta$ ,  $\beta$ , and  $\gamma$  correspond to rotations around  $\mathbf{v}$ ,  $\mathbf{t}$ , and  $\mathbf{k}$ , respectively, and  $l_{NP}$  is the distance between the points  $P$  and  $N$ , where  $\mathbf{t} \cdot \mathbf{v} = 0$ . Set  $\mathbf{P}_0 = [0, 0, 0, 0]^T$  as the initial configuration of the GSLPM-RCM, where,  $\mathbf{t} = [1, 0, 0]^T$  and  $\mathbf{b} = [0, 1, 0]^T$ . Following the design principle of the GSLPM-RCM, the position of the point  $B_i$  determines the position and orientation of the output link. The rotation matrix from  $\{\mathbf{L}_i\}$  to  $\{\mathbf{G}\}$  is formulated as follows:

$${}^G\mathbf{R}_{L_i} = \mathbf{R}_w(\alpha_i) \mathbf{R}_{y_i}(t) = \begin{bmatrix} c\alpha_i & -s\alpha_i & 0 \\ s\alpha_i & c\alpha_i & 0 \\ 0 & 0 & 1 \end{bmatrix} \begin{bmatrix} ct & 0 & st \\ 0 & 1 & 0 \\ -st & 0 & ct \end{bmatrix} = \begin{bmatrix} c\alpha_i ct & -s\alpha_i & c\alpha_i st \\ s\alpha_i ct & c\alpha_i & s\alpha_i st \\ -st & 0 & ct \end{bmatrix} \quad (1)$$

where symbols  $s$  and  $c$  are sine and cosine functions, respectively.

### 3. Kinematics and workspace analysis

#### 3.1. Inverse kinematics

Based on the modular analysis method, the inverse kinematics analysis of the GSLPM-RCM is divided into three parts: the reconfigurable base, limb- $i$ , and SCS.

##### (a) SCS

According to the length geometric relation, the distance between the points  $N$  and  $G$  is derived as

$$l_{GN} = l_{NP} + l_{FP} - l_{GE} - 2l_1 l_{GE} / l_2 \quad (2)$$

where  $l_1$  and  $l_2$  represent the length of the link  $I_iE$  and link  $B_iE$ , respectively; The distance between the points  $N$  and  $P$  ( $G$  and  $E$ ,  $F$  and  $P$ ) is  $l_{NP}$  ( $l_{GE}$ ,  $l_{FP}$ ). Considering the  $z$ -coordinate of point  $P$  is negative when the reference point  $P$  is below the  $xNy$ -plane, in this instance,  $l_{NP}$  is defined as negative, and vice versa. For a right triangle, yields:

$$r^2 = l_{GN}^2 + \left( \frac{l_{B_1B_2}}{2} \right)^2 \quad (3)$$

Combining Eqs. (2) and (3), we get:

$$\begin{cases} l_{GE} = \frac{-E_2 \pm \sqrt{E_2^2 - 4E_1E_3}}{2E_1} \\ l_{B_1B_2} = 2\sqrt{l_2^2 - l_{GE}^2} \end{cases} \quad (4)$$

where

$$\begin{cases} E_1 = 4l_1^2 + 4l_1l_2, \\ E_2 = -4l_1l_2l_{FP} - 4l_1l_2l_{NP} - 2l_2^2l_{FP} - 2l_2^2l_{NP}, \\ E_3 = -r^2l_2^2 + l_2^4 + l_2^2l_{FP}^2 + l_2^2l_{NP}^2 + 2l_2^2l_{FP}l_{NP}. \end{cases}$$

In the frame  $\{G\}$ , through rotation transformation,  $\mathbf{k}$  and  $\mathbf{b}$  can be expressed as

$$\begin{cases} \mathbf{k} = \mathbf{R}_v(\theta) \mathbf{R}_t(\beta) \cdot \mathbf{w} = [c\beta s\theta, -s\beta, c\beta c\theta]^T \\ \mathbf{b} = \mathbf{R}_v(\theta) \mathbf{R}_t(\beta) \cdot \mathbf{R}_k(\gamma) \cdot \mathbf{v} = [s\theta s\beta c\gamma - c\theta s\gamma, c\beta s\gamma, c\theta s\beta c\gamma + s\theta s\gamma]^T \end{cases} \quad (5)$$

where in

$$\mathbf{R}_v(\theta) = \begin{bmatrix} c\theta & 0 & s\theta \\ 0 & 1 & 0 \\ -s\theta & 0 & c\theta \end{bmatrix}, \quad \mathbf{R}_t(\beta) = \begin{bmatrix} 1 & 0 & 0 \\ 0 & c\beta & -s\beta \\ 0 & s\beta & c\beta \end{bmatrix}, \quad \mathbf{R}_k(\gamma) = \begin{bmatrix} c\gamma & -s\gamma & 0 \\ s\gamma & c\gamma & 0 \\ 0 & 0 & 1 \end{bmatrix}.$$

Based on the vector closed-loop equation, the input of the SCS can be written as

$$\mathbf{b}_i = l_{GN}\mathbf{k} + (-1)^i \frac{l_{B_1B_2}}{2} \mathbf{b} = [b_{ix}, b_{iy}, b_{iz}]^T \quad (6)$$

(b) Limb- $i$

The position vector  $\mathbf{b}_i$  of the point  $B_i$  at  $\{G\}$  is formulated as

$$\mathbf{b}_i = {}^G\mathbf{R}_{Li} \cdot \mathbf{R}_{a_i}(\theta_i) \mathbf{R}_{t_i}(\beta_i) \cdot r\mathbf{w} \quad (7)$$

where

$$\mathbf{R}_{a_i}(\theta_i) = \begin{bmatrix} 1 & 0 & 0 \\ 0 & c\theta_i & -s\theta_i \\ 0 & s\theta_i & c\theta_i \end{bmatrix}, \quad \mathbf{R}_{t_i}(\beta_i) = \begin{bmatrix} c\beta_i & 0 & s\beta_i \\ 0 & 1 & 0 \\ -s\beta_i & 0 & c\beta_i \end{bmatrix}$$

Both sides of Eq. (7) left multiplied by the inverse of  ${}^G\mathbf{R}_{Li}$  yields:

$${}^G\mathbf{R}_{Li}^{-1} \cdot \mathbf{b}_i = \mathbf{R}_{a_i}(\theta_i) \mathbf{R}_{t_i}(\beta_i) \cdot r\mathbf{w} = [rs\beta_i, -rs\theta_i c\beta_i, rc\theta_i c\beta_i]^T \quad (8)$$

Let

$$\mathbf{d}_i = {}^G\mathbf{R}_{Li}^{-1} \cdot \mathbf{b}_i = [d_{ix}, d_{iy}, d_{iz}]^T \quad (9)$$

The input angles of the limb- $i$  are solved as

$$\begin{cases} \theta_i = \tan^{-1}(-d_{iy}/d_{iz}) \\ \beta_i = \sin^{-1}(d_{ix}/r) \end{cases} \quad (10)$$

where  $\tan^{-1}$  is arctangent function, and  $\sin^{-1}$  is arcsine function. Then, two motor angles of the limb- $i$  are obtained as

$$\begin{cases} \varphi_{i1} = \theta_i/k \\ \varphi_{i2} = \beta_i \end{cases} \quad (11)$$

where  $k$  is the transmission ratio of the synchronous belt transmission.

(c) The reconfigurable base

The reconfigurable base is actuated by a P joint allowing for a simplified kinematics diagram as depicted in Figure 2(e).  $l_{GO}$  represents the distance between points G and O,  $l_{NA}$  represents the distance



between points A and N,  $l_{GH}$  and  $l_{HF}$  denote GH and HF segments of the link FH, respectively, and  $l_{OH}$  corresponds to the length of the link OH. Applying the law of cosines, the distance  $l_{GO}$  can be derived as

$$l_{GO} = l_{OH}c\alpha \pm \sqrt{l_{OH}^2 c^2 \alpha - l_{OH}^2 + l_{GH}^2} \quad (12)$$

Utilizing the properties of similar triangles, the position vector of RCM point N in  $\{O\}$  is derived as

$$\mathbf{n} = [l_{NA}l_{GO}/l_{OH}, 0, 0]^T \quad (13)$$

### 3.2. Workspace

The workspace is a significant feature of PMs, determining the type of operation task and serving as a foundation for planning robot motion trajectories. To determine the reachable workspace, the reachable extent of limbs and the SCS need to be assessed. Furthermore, the conditions for rising interference between the limb and the SCS also need to be determined. According to the structure of the GSLPM-RCM, the reachable extent of the limbs corresponds to the output range for the limb, denoted as  $\theta_i \in (\theta_i^{\min}, \theta_i^{\max})$  and  $\beta_i \in (\beta_i^{\min}, \beta_i^{\max})$ , where  $\theta_i^{\min}$ ,  $\theta_i^{\max}$ ,  $\beta_i^{\min}$ , and  $\beta_i^{\max}$  represent the limiting output values of limb- $i$ , occurring when collisions are detected between the links. Similarly, the reachable extent of the SCS is determined by  $l_{B1B2}$ , expressed as  $l_{B1B2} \in (l_{B1B2}^{\min}, l_{B1B2}^{\max})$ , where  $l_{B1B2}^{\min}$  and  $l_{B1B2}^{\max}$  correspond to the distances between points  $B_1$  and  $B_2$  when the links of the SCS collide. Whether interference between the limb and the SCS occurs can be determined by examining the angle between the two planes where limb- $i$  and the SCS are respectively situated, i.e.,

$$\delta_{P_i} = \cos^{-1}(\mathbf{n}_{L_i} \cdot \mathbf{n}_{SCS}) < \delta_{P_i}^{\max} \quad (14)$$

where  $\mathbf{n}_{L_i} = (\mathbf{b}_i \times \mathbf{a}_i)/\|\mathbf{b}_i \times \mathbf{a}_i\|$  and  $\mathbf{n}_{SCS} = (\mathbf{k} \times \mathbf{b})/\|\mathbf{k} \times \mathbf{b}\|$  are the unit normal vectors of the planes where the limb- $i$  and the SCS are situated, respectively.  $\delta_{P_i}^{\max}$  is the limit angle when limb- $i$  and the SCS collide.

With the different central angle  $2\alpha$ , the workspace of the GSLPM-RCM is analyzed based on the inverse kinematics. Through analysis, it was found that there is not much difference between the orientation workspace with different  $l_{NP}$ , which can be verified by the results of ref. [13]. In this work, the orientation workspaces with  $l_{NP} = -260$  mm are drawn as shown in Figure 5. It is observed that the orientation workspace demonstrates symmetry about the plane- $XZ$ , as indicated by the boundary of angle  $\gamma$  in Figure 5. To provide a quantitative description of the workspace dimensions, a maximum inscribed circle within the boundary of angle  $\gamma$  is introduced, as depicted in Figure 6. The boundary value  $\gamma_B$  of the angle  $\gamma$  and the radius  $r_B$  of the maximum inscribed circle are utilized as indices to characterize the workspace. As the central angle  $2\alpha$  decreases, it is necessary to reduce  $\gamma_B$  to obtain a larger  $r_B$ .

## 4. Motion/force transmissibility

Although this RCM manipulator contains a reconfigurable base, the reconfigurable base does not alter the motion characteristic of the manipulator, so the performance analysis of the mechanism can be transformed into an analysis of GLSPM-RCM with a rigid base. According to the method proposed in the literature [43] for singularity analysis of parallel manipulators, the motion/force transmissibility for the GLSPM-RCM is reformulated considering its structural characteristics.

### 4.1. Transmission wrenches of the GSLPM-RCM

In the GSLPM-RCM, the output of limb- $i$  is represented by the vector  $\mathbf{b}_i$ . The output link of the SCS exhibits three rotational degrees of freedom and one translational degree of freedom centered around

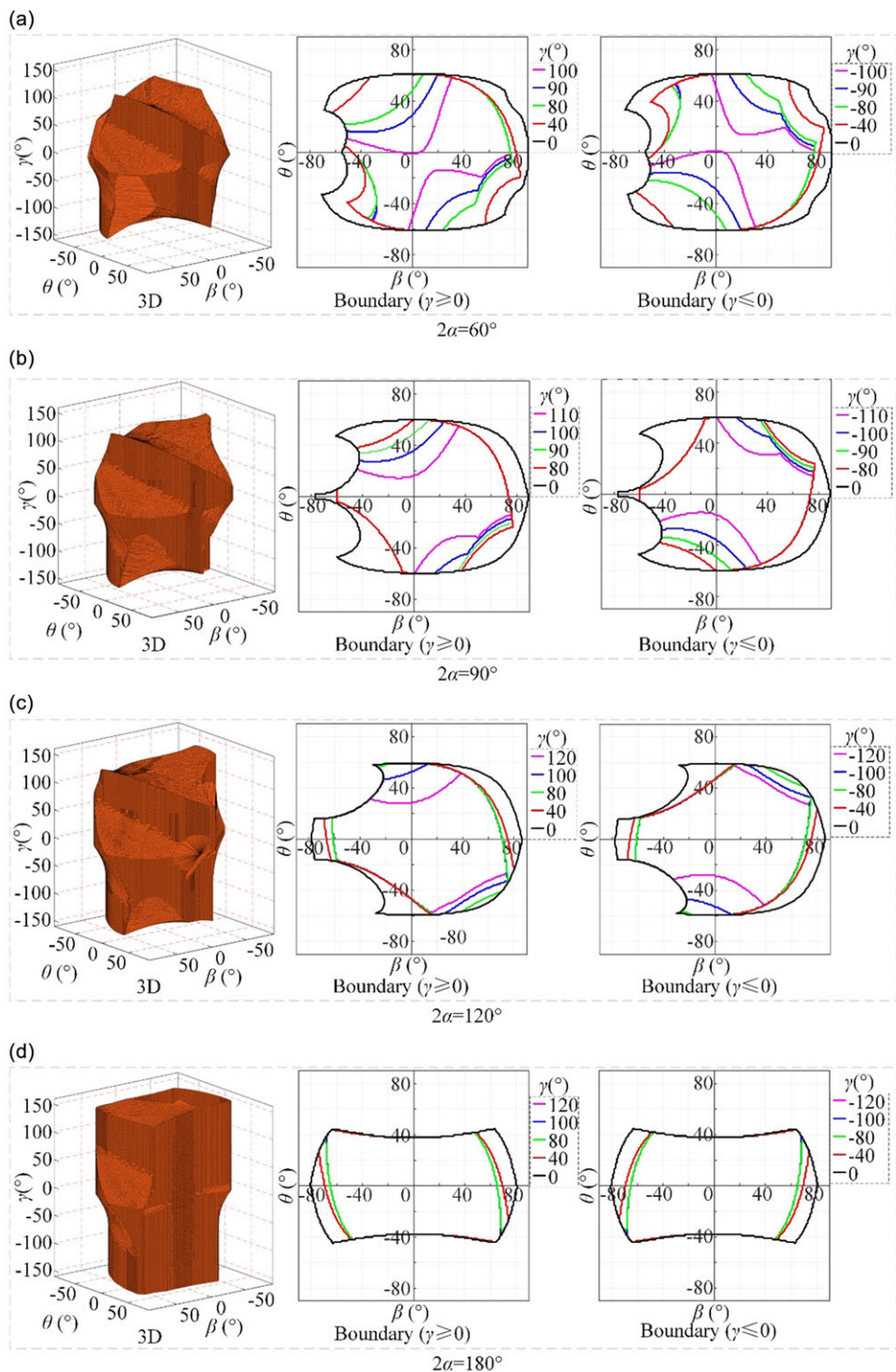


**Figure 5.** The orientation workspace with  $l_{NP} = -260$  mm.



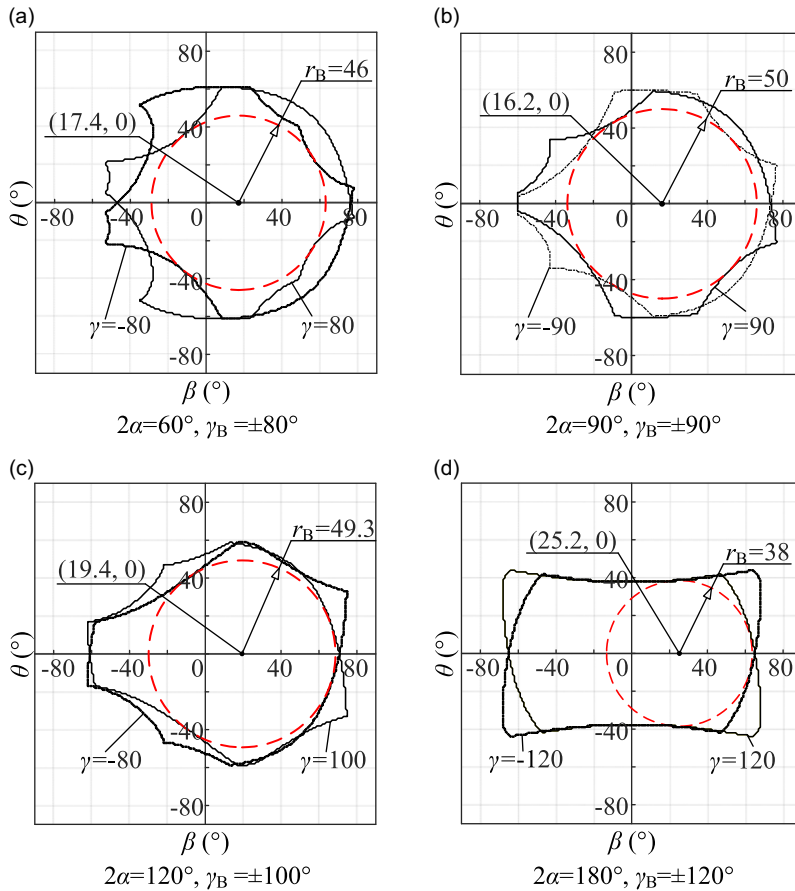


**Figure 6.** The description of the size of the workspace.

point N. To facilitate analysis, a simplified equivalent model of the GSLPM-RCM is constructed, reflecting its inherent characteristics as depicted in Figure 7. This simplified mechanism comprises two limbs with a  $R^{ai}R^{ti}R^{bi}R^gR^g$ -structure, where the three axes  $\mathbf{a}_i$ ,  $\mathbf{t}_i$ , and  $\mathbf{b}_i$  intersect at point N, and  $i = 1, 2$ . Additionally, a virtual middle limb with an  $R^pR^kP^k$ -structure is introduced to constrain the output link. Each limb in the GSLPM-RCM features two actuated joints, which are arranged in series and mounted near the base.

Within the frame  $\{\mathcal{G}\}$ , the twist system for limb- $i$  is written as

$$\{\mathcal{S}_i\} = \begin{cases} \mathcal{S}_{i,1} = (\mathbf{a}_i; \mathbf{0}) \\ \mathcal{S}_{i,2} = (\mathbf{t}_i; \mathbf{0}) \\ \mathcal{S}_{i,3} = (\mathbf{b}_i/r; \mathbf{0}) \\ \mathcal{S}_{i,4} = (\mathbf{g}; \mathbf{b}_i \times \mathbf{g}) \\ \mathcal{S}_{i,5} = (\mathbf{g}; l_{EN}\mathbf{k} \times \mathbf{g}) \end{cases} \quad (15)$$

where  $\mathbf{g} = \mathbf{b} \times \mathbf{k}$ . The twist system  $\{\mathcal{S}_i\}$  is a 5-system. The twists corresponding to each joint in limb- $i$  are denoted by  $\mathcal{S}_{i,1}$ ,  $\mathcal{S}_{i,2}$ ,  $\mathcal{S}_{i,3}$ ,  $\mathcal{S}_{i,4}$ , and  $\mathcal{S}_{i,5}$ , and  $\mathcal{S}_{i,1}$  and  $\mathcal{S}_{i,2}$  are input twists of limb- $i$ . By applying the principle of reciprocity, the corresponding constraint wrenches for Eq. (15) is calculated as

$$\{\mathcal{S}'_i\} = \mathcal{S}'_i = (\mathbf{g}; \mathbf{0}) \quad (16)$$

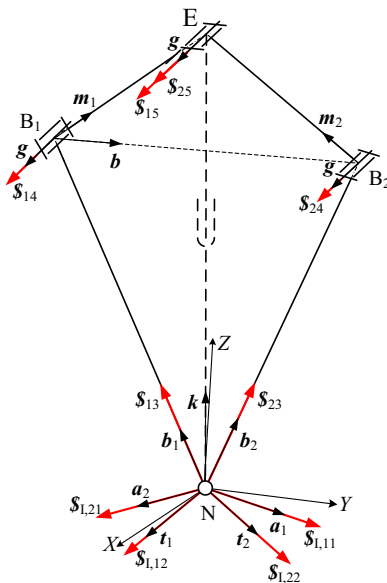


**Figure 7.** A simplified equivalent model of the GSLPM-RCM.

$\$i^r$  is a pure force along  $\mathbf{g}$  passing through point N. Because limb- $i$  contains two actuated joints, and the  $i1^{\text{th}}$  and  $i2^{\text{th}}$  actuated joints are connected in series and move independently, the transmission wrenches associated with two actuated joints in limb- $i$  need to be derived, respectively. For the transmission wrench associated with the  $i1^{\text{th}}$  actuated joint, it is reciprocal to all the twists of joints in limb- $i$  except for  $\$_{lil}$ , i.e.,

$$\mathcal{S}_{T, i1} \circ \mathcal{S}_{ij} = 0 \left( \mathcal{S}_{ij} \in \{\mathcal{S}_{L, i2}, \mathcal{S}_{i3}, \mathcal{S}_{i4}, \mathcal{S}_{i5}\} \right) \quad (17)$$

To find the transmission wrench  $\$_{T,i1}$  accurately, two planes are constructed using limb-1 as an example as shown in Figure 8(a). In Figure 8(a), the plane  $P_{i1}$  is formed by the twists  $\$_{i,2}$  and  $\$_{i,3}$  and determined by the unit vectors  $\mathbf{t}_i$  and  $\mathbf{b}_i$ . The plane  $P_{i3}$  is formed by the twists  $\$_{i,4}$  and  $\$_{i,5}$  and determined by the unit vectors  $\mathbf{g}$  and  $\mathbf{m}_i$ . The intersecting line  $L_{i1}$  of the planes  $P_{i1}$  and  $P_{i3}$  corresponds to the desired transmission wrench  $\$_{T,i1}$  associated with the  $i1^{\text{th}}$  actuated joint. The transmission wrench  $\$_{T,i1}$  is a pure force, and it can be derived as

$$\mathbf{s}_{\text{T},i1} = (\mathbf{f}_i; \mathbf{b}_i \times \mathbf{f}_i) \quad (18)$$

where the unit vector  $\mathbf{f}_i$  is the directional vector of the intersecting line  $L_{i1}$ , and  $\mathbf{f}_i = ((\mathbf{g} \times \mathbf{m}_i) \times (\mathbf{b}_i/r \times \mathbf{t}_i)) / |(\mathbf{g} \times \mathbf{m}_i) \times (\mathbf{b}_i/r \times \mathbf{t}_i)|$ , the unit vector  $\mathbf{m}_i$  is the directional vector of the link B $_i$ E, and  $\mathbf{m}_i = (l_{EN}\mathbf{k} - \mathbf{b}_i)/l_2$ .

Similarly, for the transmission wrench associated with the  $i2^{\text{th}}$  actuated joint, the following reciprocal relationship exists, i.e.,

$$\$_{T,i2} \circ \$_{ij} = 0 \left( \$_{ij} \in \{ \$_{1,i1}, \$_{i3}, \$_{i4}, \$_{i5} \} \right) \quad (19)$$

The transmission wrench  $\$_{T,i2}$  can be found according to Figure 8(b). In Figure 8(b), the plane  $P_{i2}$  is formed by the twists  $\$_{L,i1}$  and  $\$_{i3}$  and determined by the unit vectors  $\mathbf{a}_i$  and  $\mathbf{b}_i$ . The transmission wrench  $\$_{T,i2}$  associated with the  $i2^{\text{th}}$  actuated joint along the intersecting line  $L_{i2}$  of the planes  $P_{i2}$  and  $P_{i3}$ , and it is a pure force and can be derived as

$$\mathbf{\$}_{\text{T},l2} = (\mathbf{h}_i; \mathbf{b}_i \times \mathbf{h}_i) \quad (20)$$



$$K_{i1,3} = \frac{A_{i1,3}B_{i1,2}D_{i1,1} - A_{i1,2}B_{i1,3}D_{i1,1} - A_{i1,3}B_{i1,1}D_{i1,2} + A_{i1,1}B_{i1,3}D_{i1,2} + A_{i1,2}B_{i1,1}D_{i1,3} - A_{i1,1}B_{i1,2}D_{i1,3}}{A_{i1,3}B_{i1,2}C_{i1,1} - A_{i1,2}B_{i1,3}C_{i1,1} - A_{i1,3}B_{i1,1}C_{i1,2} + A_{i1,1}B_{i1,3}C_{i1,2} + A_{i1,2}B_{i1,1}C_{i1,3} - A_{i1,1}B_{i1,2}C_{i1,3}},$$

$$\chi_{i1} = \pm 1 / \sqrt{K_{i1,1}^2 + K_{i1,2}^2 + K_{i1,3}^2}.$$

The symbol “ $\neg i$ ” represents that it is not  $i$ . Because  $i = 1$  or  $2$ , if  $i$  is  $1$ , then “ $\neg i$ ” is  $2$ ; if  $i$  is  $2$ , then “ $\neg i$ ” is  $1$ . Similarly, the output twist  $\$_{O,i2}$  associated with the  $i2^{\text{th}}$  actuated joint is derived as

$$\$_{O,i2} = (s_{i2}; \chi_{i2}\mathbf{k}) \quad (24)$$

where

$$s_{i2} = \chi_{i2} [K_{i2,1}, K_{i2,2}, K_{i2,3}]^T;$$

$$A_{i2,1} = \mathbf{u} \cdot (\mathbf{b}_i \times \mathbf{f}_i), B_{i2,1} = \mathbf{v} \cdot (\mathbf{b}_i \times \mathbf{f}_i), C_{i2,1} = \mathbf{w} \cdot (\mathbf{b}_i \times \mathbf{f}_i), D_{i2,1} = -\mathbf{k} \cdot \mathbf{f}_i;$$

$$A_{i2,2} = \mathbf{u} \cdot (\mathbf{b}_{\neg i} \times \mathbf{f}_{\neg i}), B_{i2,2} = \mathbf{v} \cdot (\mathbf{b}_{\neg i} \times \mathbf{f}_{\neg i}), C_{i2,2} = \mathbf{w} \cdot (\mathbf{b}_{\neg i} \times \mathbf{f}_{\neg i}), D_{i2,2} = -\mathbf{k} \cdot \mathbf{f}_{\neg i};$$

$$A_{i2,3} = \mathbf{u} \cdot (\mathbf{b}_{\neg i} \times \mathbf{h}_{\neg i}), B_{i2,3} = \mathbf{v} \cdot (\mathbf{b}_{\neg i} \times \mathbf{h}_{\neg i}), C_{i2,3} = \mathbf{w} \cdot (\mathbf{b}_{\neg i} \times \mathbf{h}_{\neg i}), D_{i2,3} = -\mathbf{k} \cdot \mathbf{h}_{\neg i};$$

$$K_{i2,1} = \frac{B_{i2,3}C_{i2,2}D_{i2,1} - B_{i2,2}C_{i2,3}D_{i2,1} - B_{i2,3}C_{i2,1}D_{i2,2} + B_{i2,1}C_{i2,3}D_{i2,2} + B_{i2,2}C_{i2,1}D_{i2,3} - B_{i2,1}C_{i2,2}D_{i2,3}}{A_{i2,3}B_{i2,2}C_{i2,1} - A_{i2,2}B_{i2,3}C_{i2,1} - A_{i2,3}B_{i2,1}C_{i2,2} + A_{i2,1}B_{i2,3}C_{i2,2} + A_{i2,2}B_{i2,1}C_{i2,3} - A_{i2,1}B_{i2,2}C_{i2,3}},$$

$$K_{i2,2} = \frac{-A_{i2,3}C_{i2,2}D_{i2,1} + A_{i2,2}C_{i2,3}D_{i2,1} + A_{i2,3}C_{i2,1}D_{i2,2} - A_{i2,1}C_{i2,3}D_{i2,2} - A_{i2,2}C_{i2,1}D_{i2,3} + A_{i2,1}C_{i2,2}D_{i2,3}}{A_{i2,3}B_{i2,2}C_{i2,1} - A_{i2,2}B_{i2,3}C_{i2,1} - A_{i2,3}B_{i2,1}C_{i2,2} + A_{i2,1}B_{i2,3}C_{i2,2} + A_{i2,2}B_{i2,1}C_{i2,3} - A_{i2,1}B_{i2,2}C_{i2,3}},$$

$$K_{i2,3} = \frac{A_{i2,3}B_{i2,2}D_{i2,1} - A_{i2,2}B_{i2,3}D_{i2,1} - A_{i2,3}B_{i2,1}D_{i2,2} + A_{i2,1}B_{i2,3}D_{i2,2} + A_{i2,2}B_{i2,1}D_{i2,3} - A_{i2,1}B_{i2,2}D_{i2,3}}{A_{i2,3}B_{i2,2}C_{i2,1} - A_{i2,2}B_{i2,3}C_{i2,1} - A_{i2,3}B_{i2,1}C_{i2,2} + A_{i2,1}B_{i2,3}C_{i2,2} + A_{i2,2}B_{i2,1}C_{i2,3} - A_{i2,1}B_{i2,2}C_{i2,3}},$$

$$\chi_{i2} = \pm 1 / \sqrt{K_{i2,1}^2 + K_{i2,2}^2 + K_{i2,3}^2}.$$

## 4.2. Transmission index of the GSLPM-RCM

In ref. [43], Liu. et al. introduced the input, output, and local transmission index (ITI, OTI, and LTI). For the GSLPM-RCM, firstly, the transmission index of each limb is characterized by taking the smaller of the transmission indices associated with its two actuated joints. That is,

$$\eta_{l,i} = \min_{k=1,2} \left( \frac{|\$_{l,ik} \circ \$_{T,ik}|}{|\$_{l,ik} \circ \$_{T,ik}|_{\max}} \right) \quad (25)$$

$$\eta_{O,i} = \min_{k=1,2} \left( \frac{|\$_{T,ik} \circ \$_{O,ik}|}{|\$_{T,ik} \circ \$_{O,ik}|_{\max}} \right) \quad (26)$$

Then, the local and global transmission indices for the GSLPM-RCM are written as

$$\eta_{LTI} = \min_{i=1,2} \{\eta_{l,i}, \eta_{O,i}\} \quad (27)$$

$$\tau_{GTI} = \frac{\int_W \eta_{LTI} dW}{\int_W dW} \quad (28)$$

## 5. Optimization design

The optimal design seeks to identify a set of ideal structural parameters that enhance the performance of the mechanism. This problem can be defined mathematically as

$$\begin{aligned} &\text{Find a vector } \mathbf{Y} = [y_1, y_1, \dots, y_n]^T \\ &\text{that max } \mathbf{G}(\mathbf{Y}) = [\mathbf{g}_1(\mathbf{Y}), \mathbf{g}_2(\mathbf{Y}), \dots, \mathbf{g}_m(\mathbf{Y})]^T \\ &\text{with } h_1(\mathbf{Y}) \geq 0 \text{ and } h_2(\mathbf{Y}) = 0 \end{aligned} \quad (29)$$

**Table I.** Optimal design parameters.

| No. | Design variables |             |          |            |            |               | Indices      |             |
|-----|------------------|-------------|----------|------------|------------|---------------|--------------|-------------|
|     | $\alpha$ (°)     | $\iota$ (°) | $r$ (mm) | $l_1$ (mm) | $l_2$ (mm) | $l_{FP}$ (mm) | $\tau_{GTI}$ | $\tau_{RW}$ |
| 1   | 60               | 14.94       | 261.23   | 165.17     | 176.52     | 571.34        | 0.390        | 36.620      |
| 2   | 60               | 4.24        | 217.82   | 230.56     | 113.81     | 571.29        | 0.426        | 42.294      |
| 3   | 60               | 9.6         | 195.09   | 134.89     | 115.08     | 495.67        | 0.351        | 40.505      |
| 4   | 60               | 9.1         | 247.55   | 123.24     | 176.03     | 568.51        | 0.336        | 43.848      |
| 5   | 60               | 14.21       | 258.72   | 167.96     | 141.45     | 564.33        | 0.344        | 43.311      |

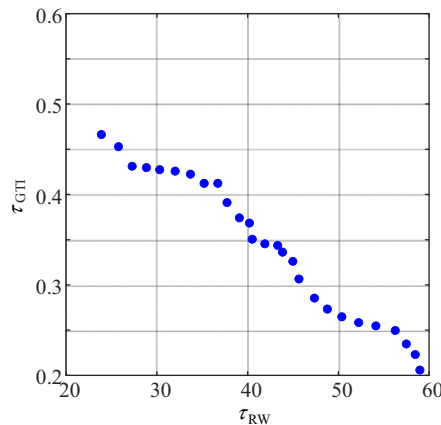


**Figure 9.** Pareto fronts.

where  $\mathbf{Y} \in \mathbb{R}^n$  is vector of the design variables, and  $\mathbf{G} \in \mathbb{R}^m$  is the multi-objective functions,  $h_i(\bullet)$  is constraint condition. For the GSLPM-RCM, besides the GTI index, the regular workspace (RW) index is also presented, i.e.,  $\tau_{RW} = r_B$ , where  $r_B$  is defined in Section 3.2. Then,  $\mathbf{Y}$  and  $\mathbf{G}$  are defined as

$$\begin{cases} \mathbf{Y} = [\iota, r, l_1, l_2, l_{FP}]^T \\ \mathbf{G} = [\tau_{GTI}, \tau_{RW}]^T \end{cases} \quad (30)$$

where  $l_{FP}$  is the length of output link FP. The constraint conditions are set as

$$\begin{cases} \iota \in [0, 30^\circ], \\ r \in (0, 300), l_1 \in (0, 300), l_2 \in (0, 300), l_{FP} \in (400, 700) \\ l_1 < l_2 \\ \sqrt{r^2 - l_1^2} + h \leq l_{FP} \leq l_1 + 2l_2 + r \end{cases} \quad (31)$$

where  $h = 280$  mm is the maximum distance between points P and N. With the reconfigurable parameter  $2\alpha = 120^\circ$ , the optimized solutions are found by SPEA-II. Pareto fronts are drawn as illustrated in Figure 9. Five sets of candidate optimal design parameters are listed in Table I.

Based on Table I, a set of structural parameters is selected for designing the GSLPM-RCM, i.e.,  $[5^\circ, 220$  mm, 230 mm, 110 mm, 570 mm]. To facilitate the representation of the distribution of LTI, the angles  $(\theta, \beta)$  are transformed into the Tilt-and-Torsion (T&T) angles  $(\kappa, \nu)$  [47], following the methodology outlined in ref. [13]. For a given position of reference point P in the workspace (determined by  $\kappa, \nu$ , and  $l_{NP}$ ), the output link FP can rotate around its axis  $\mathbf{k}$  within a certain range  $[\gamma_{min}, \gamma_{max}]$ . The average of the LTI with possible rotation angle  $\gamma$  is calculated to assess the transmissibility of the manipulator at a given position of reference point P. Figure 10 displays the distribution of LTI with different  $l_{NP}$  and the reconfigurable parameter  $2\alpha$ . Figure 11(a) shows the relationship between the global transmission index

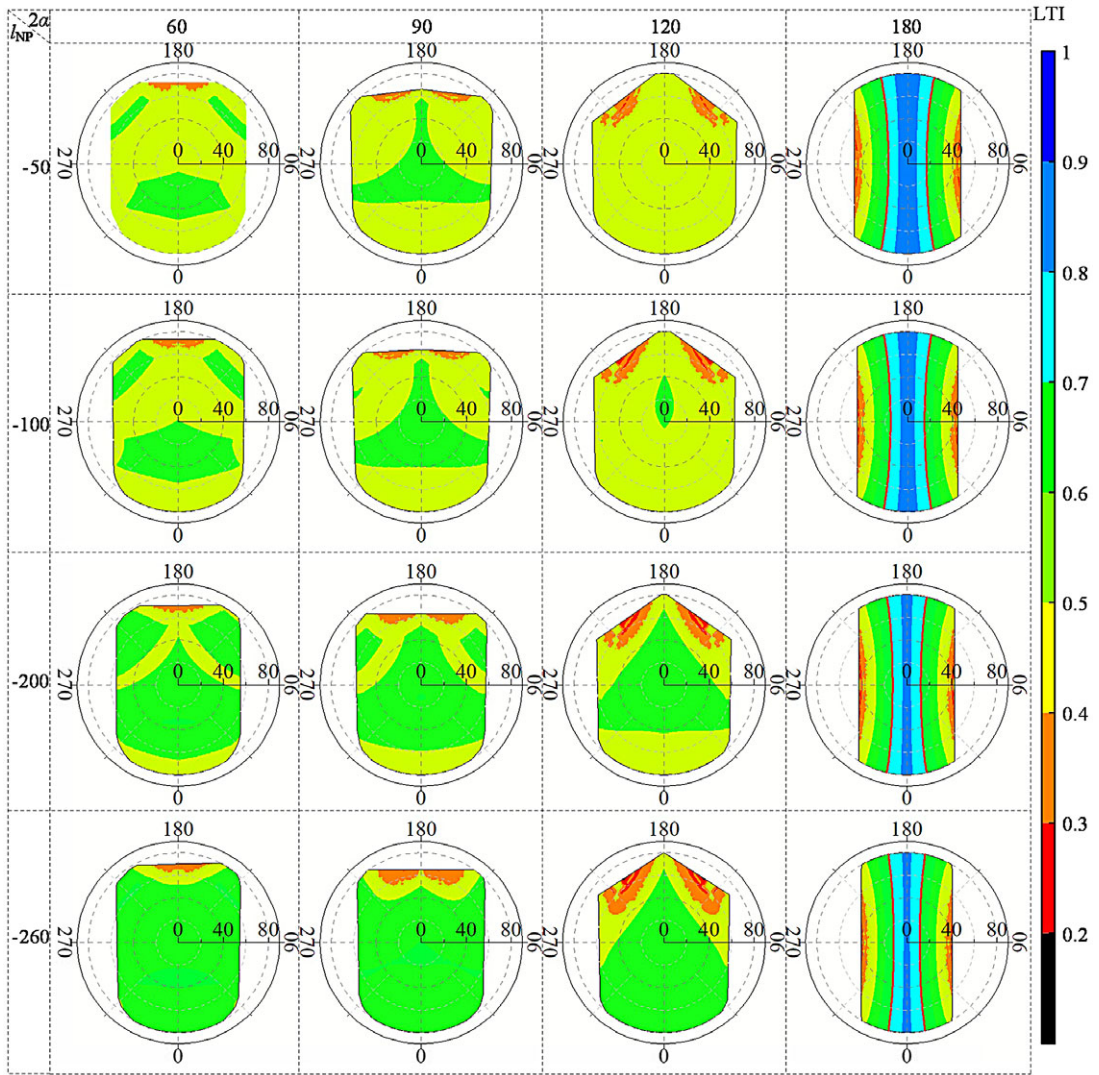


**Figure 10.** The distribution of LTI with different  $l_{NP}$  and reconfigurable parameter  $2\alpha$ .

and the reconfigurable parameter  $2\alpha$ . The results indicate that for the manipulator with the different reconfigurable parameter  $2\alpha$ , the corresponding global transmission indices are greater than 0.4. When  $2\alpha > 145^\circ$ , the manipulator has good global transmission performance. Figure 11(b) shows the variation of workspace index  $\tau_{RW}$  of the manipulator with reconfigurable parameters. The boundary value of the angle  $\gamma$  can all reach over  $100^\circ$ , i.e.,  $\gamma_B \geq 100^\circ$ , here the radius of the maximum inscribed circle of the boundary is all greater than  $40^\circ$ , i.e.,  $r_B > 40^\circ$ . The regular workspace can be within a circle with a radius exceeding  $40^\circ$ .

## 6. Conclusions

In this paper, a generalized single-loop parallel RCM manipulator with a reconfigurable base is presented based on a spherical surface geometrical model. Structurally, the proposed manipulator features a



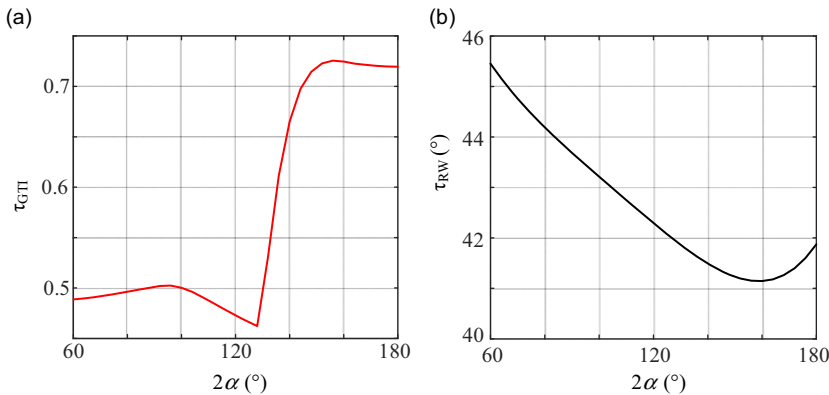


**Figure 11.** The relationship between indices and  $2\alpha$ : (a)  $\tau_{GTI}$  and (b)  $\tau_{RW}$ .

simplified structure and a large workspace due to its single-loop configuration. Additionally, the manipulator can adapt its characteristics to meet various task requirements by adjusting the parameters of the reconfigurable base, such as for multi-robot cooperative operations. Significantly, the manipulator presented differs from traditional parallel mechanisms, which necessitates a reformulation of the motion/force transmissibility analysis. By evaluating the derived transmissibility indices and the defined workspace index, the structural parameters of the mechanism are optimized. Furthermore, alterations in the reconfigurable parameters significantly affect both the workspace shape and the distribution of the LTI. According to the workspace shape and the distribution of LTI, the reconfigurable parameters of the manipulator can be adjusted, and the motion trajectory can be planned more reasonably so that the manipulator can better adapt to different tasks.

**Author contribution.** Luquan Li: Writing – original draft, Validation, Investigation, Formal analysis. Chunxu Tian: Validation, Resources, Formal analysis. Zhihao Xia: Resources, Formal analysis. Dan Zhang: Writing – review & editing, Validation, Supervision, Conceptualization.

**Financial support.** Luquan Li thanks the support of the China Postdoctoral Science Foundation (Grant No. 2023M740663). Chunxu Tian thanks the support of the National Nature Science Foundation of China (Grant No. 52305012). Dan Zhang thanks the support of the Research Institute for Artificial Intelligence of Things (RIAIoT) at the Hong Kong Polytechnic University and the Nature Science Foundation of China (Grant No. 52150710538).

**Competing interests.** The authors declare that they have no known competing financial interests or personal relationships that could have appeared to influence the work reported in this paper.

**Ethical approval.** Not applicable.

## References

- [1] C. H. Kuo, J. S. Dai and P. Dasgupta, “Kinematic design considerations for minimally invasive surgical robots: An overview,” *Int. J. Med. Robot. Comp.* **8**(2), 127–145 (2012).
- [2] R. H. Taylor, J. Funda, B. Eldridge, S. Gomory, K. Gruben, D. LaRose, M. Talamini, L. Kavoussi and J. Anderson, “A telerobotic assistant for laparoscopic surgery,” *IEEE Eng. Med. Biol.* **14**(3), 279–288 (1995).
- [3] G. Zong, X. Pei, J. Yu and S. Bi, “Classification and type synthesis of 1-DOF remote center of motion mechanisms,” *Mech. Mach. Theory* **43**(12), 1585–1595 (2008).
- [4] H.-C. Hsieh, D.-F. Chen, L. Chien and C.-C. Lan, “Design of a parallel actuated exoskeleton for adaptive and safe robotic shoulder rehabilitation,” *IEEE/ASME Trans. Mechatron.* **22**(5), 2034–2045 (2017).
- [5] G. Chen, J. Wang and H. Wang, “A new type of planar two degree-of-freedom remote center-of-motion mechanism inspired by the Peaucellier-Lipkin straight-line linkage,” *J. Mech. Design* **141**(1), 015001 (2019).

- [6] J. Wu, T. Wang, H. Guo, Y. Wang, D. Guo, B. Lu, Z. Wang, F. Zhong, H. Wang, J. Yuan, Y. Li, T. H. Cheung, Y. Wang and Y.-H. Liu, "Design, control, and experiments of a novel robotic uterine manipulator with the motorized 3-DoF manipulation rod," *IEEE Trans. Biomed. Eng.* **70**(7), 2203–2214 (2023).
- [7] Y. Yang, H. Liu, H. Zheng, Y. Peng and Y. Yu, "Two types of remote-center-of-motion deployable manipulators with dual scissor-like mechanisms," *Mech. Mach. Theory* **160**, 104274 (2021).
- [8] S. Nisar, T. Endo and F. Matsuno, "Design and optimization of a 2-degree-of-freedom planar remote center of motion mechanism for surgical manipulators with smaller footprint," *Mech. Mach. Theory* **129**, 148–161 (2018).
- [9] J. Li, J. Wang, J. Zhao and W. G. Design, "Dimensional synthesis and evaluation of a novel 2-DOF spherical RCM mechanism for minimally invasive surgery," *J. Mech. Robotics* **16**(5), 051005 (2024).
- [10] H. C. Chen, W. J. Su and C. W. Chen, "A novel microsurgical robot with double-parallelogram RCM mechanism and back-driven instrument translation," *IFAC PapersOnline* **53**(2), 15940–15945 (2020).
- [11] J. Li, Y. Xing, K. Liang and S. Wang, "Kinematic design of a novel spatial remote center-of-motion mechanism for minimally invasive surgical robot," *J. Med. Devices* **9**(1), 011003 (2015).
- [12] B. Eldridge, K. Gruben, D. LaRose, J. Funda, S. Gomory, J. Karidis, G. McVicker, R. Taylor and J. Anderson, "A remote center of motion robotic arm for computer assisted surgery," *Robotica* **14**(1), 103–109 (2009).
- [13] L. Li, D. Zhang and C. Tian, "A family of generalized single-loop RCM parallel mechanisms: Structure synthesis, kinematic model, and case study," *Mech. Mach. Theory* **195**, 105606 (2024).
- [14] A. B. Aldanmaz, O. Ayit, G. Kiper and M.İ.C. Dede, "Gravity compensation of a 2R1T mechanism with remote center of motion for minimally invasive transnasal surgery applications," *Robotica* **41**(3), 807–820 (2022).
- [15] M. B. Hong, G. T. Kim and Y. H. Yoon, "ACE-ankle: A novel sensorized RCM (remote-center-of-motion) ankle mechanism for military purpose exoskeleton," *Robotica* **37**(12), 2209–2228 (2019).
- [16] P. Vischer and R. Clavel, "Argos: A novel 3-dof parallel wrist mechanism," *Int. J. Robot. Res.* **19**(1), 5–11 (2016).
- [17] G. Chen, Y. Xun, Y. Chai, S. Yao, C. Chen and H. Wang, "Design and validation of a novel planar 2R1T remote center-of-motion mechanism composing of dual-triangular and straight-line linkages," *J. Mech. Robotics*, 1–11 (2021). <https://doi.org/10.1115/1.4052339>.
- [18] Y. Wu and M. Carricato, "Line-symmetric motion generators," *Mech. Mach. Theory* **127**, 112–125 (2018).
- [19] N. B. Zhang, P. C. Huang and Q. C. Li, "Modeling, design and experiment of a remote-center-of-motion parallel manipulator for needle insertion," *Robot. Comput-Integ. Manuf.* **50**, 193–202 (2018).
- [20] N. A. Ahmadi, A. Kamali Eigoli and A. Taghvaeipour, "Adaptive backstepping controller based on a novel framework for dynamic solution of an ankle rehabilitation spherical parallel robot," *Robotica* **42**(5), 1568–1596 (2024).
- [21] T. Li and S. Payandeh, "Design of spherical parallel mechanisms for application to laparoscopic surgery," *Robotica* **20**(2), 133–138 (2002).
- [22] Y. Bian, J. Zhao, J. Li, G. Wei and J. Li, "A class of spatial remote center-of-motion mechanisms and its forward kinematics," *Robotica* **41**(3), 885–899 (2022).
- [23] L. Huang, C. Guang, Y. Yang, P. Su, H. L. Yuan, R. K. Agarwal, P. Tandon and E. X. Wang, "Type synthesis of parallel 2R1T remote center of motion mechanisms based on screw theory," *MATEC Web Conf.* **95**, 08009 (2017).
- [24] T. Yilmaz and G. Kiper, "Design and balancing of a novel 2R1T manipulator with remote center of motion. New advances in mechanisms, transmissions and applications," *Mech. Mach. Sci.* **124**, 180–188 (2023).
- [25] M. Meskini, H. Saafi, A. Mlika, M. Arsicault, S. Zeghloul and M. A. Laribi, "Development of a novel hybrid haptic (nHH) device with a remote center of rotation dedicated to laparoscopic surgery," *Robotica* **41**(10), 3175–3194 (2023).
- [26] F. Najafi and N. Sepehri, "A robotic wrist for remote ultrasound imaging," *Mech. Mach. Theory* **46**(8), 1153–1170 (2011).
- [27] C.-H. Kuo and J. S. Dai, "A Fully Decoupled Remote Center-of-Motion Parallel Manipulator for Minimally Invasive Surgery." In: *International Design Engineering Technical Conferences & Computers and Information in Engineering Conference IDETC/CIE*, Washington, USA (2011).
- [28] J. Qiu, J. Wu and B. Zhu, "Optimization design of a parallel surgical robot with remote center of motion," *Mech. Mach. Theory* **185**, 105327 (2023).
- [29] J. Liu, Z. Yang, H. Ding and M. Li, "Design and kinematical performance analysis of a novel reconfigurable parallel mechanism with three remote center-of-motion modes," *Mech. Mach. Theory* **191**, 105513 (2024).
- [30] X. Kong and C. M. Gosselin, "Type synthesis of 4-DOF SP-equivalent parallel manipulators: A virtual chain approach," *Mech. Mach. Theory* **41**(11), 1306–1319 (2006).
- [31] L. Nouaille, P. Vieyres and G. Poisson, "Process of optimisation for a 4 DOF tele-echography robot," *Robotica* **30**(7), 1131–1145 (2012).
- [32] Q. Li, J. Marie Hervé and P. Huang, "Type synthesis of a special family of remote center-of-motion parallel manipulators with fixed linear actuators for minimally invasive surgery," *J. Mech. Robotics* **9**(3), 031012 (2017).
- [33] M. Zoppi, D. Zlatanov and C. M. Gosselin, "Analytical kinematics models and special geometries of a class of 4-DOF parallel mechanisms," *IEEE Trans. Robot.* **21**(6), 1046–1055 (2005).
- [34] G. Chen, J. Wang, H. Wang, C. Chen, V. Parenti-Castelli and J. Angeles, "Design and validation of a spatial two-limb 3R1T parallel manipulator with remote center-of-motion," *Mech. Mach. Theory* **149**, 103807 (2020).
- [35] Z. Wang, W. Zhang and X. Ding, "Design and analysis of a novel metamorphic remote-centre-of-motion mechanism with parallelogram joints," *Mech. Mach. Theory* **176**, 105038 (2022).
- [36] L. J. Design, "Dimensional synthesis and evaluation of a novel 2-DOF spherical RCM mechanism for minimally invasive surgery," *J. Mech. Robot.* **16**(5), 051005 (2024).
- [37] T. Essomba, Y. Hsu, J. S. Sandoval Arevalo, M. A. Laribi and S. Zeghloul, "Kinematic optimization of a reconfigurable spherical parallel mechanism for robotic-assisted craniotomy," *J. Mech. Robot.* **11**(6), 060905 (2019).

- [38] T. Essomba and W.-H. Wang, “Design of a spherical parallel mechanism with controllable center of rotation using a spherical reconfiguration linkage,” *Mech. Mach. Theory* **199**, 105672 (2024).
- [39] A. Yaşır, G. Kiper and M.İ.C. Dede, “Kinematic design of a non-parasitic 2R1T parallel mechanism with remote center of motion to be used in minimally invasive surgery applications,” *Mech. Mach. Theory* **153**, 104013 (2020).
- [40] A. Molaei, E. Abedloo, H. D. Taghirad and Z. Marvi. Kinematic and Workspace Analysis of Diamond An Innovative Eye Surgery Robot. *In: Iranian Conference on Electrical Engineering (ICEE)*, Tehran, Iran (2015) pp. 882–887.
- [41] W. Ye, B. Zhang and Q. C. Li, “Design of a 1R1T planar mechanism with remote center of motion,” *Mech. Mach. Theory* **149**, 103845 (2020).
- [42] C. Chen and J. Angeles, “Generalized transmission index and transmission quality for spatial linkages,” *Mech. Mach. Theory* **42**(9), 1225–1237 (2007).
- [43] X. J. Liu, C. Wu and J. S. Wang, “A new approach for singularity analysis and closeness measurement to singularities of parallel manipulators,” *J. Mech. Robot.* **4**(4), 041001 (2012).
- [44] K. Chen, R. Wang, Z. Niu, P. Wang and T. Sun, “Topology design and performance optimization of six-limbs 5-DOF parallel machining robots,” *Mech. Mach. Theory* **185**, 105333 (2023).
- [45] Q. Li, N. Zhang and F. Wang, “New indices for optimal design of redundantly actuated parallel manipulators,” *J. Mech. Robot.* **9**(1), 011007 (2017).
- [46] Q. Z. Meng, F. G. Xie, X. J. Liu and Y. Takeda, “An evaluation approach for motion-force interaction performance of parallel manipulators with closed-loop passive limbs,” *Mech. Mach. Theory* **149**, 103844 (2020).
- [47] I. A. Bonev. *Geometric Analysis of Parallel Mechanisms* (Laval University, Quebec, 2002).

---

**Cite this article:** L. Li, C. Tian, Z. Xia and D. Zhang (2025). “Optimal design of a generalized single-loop parallel manipulator with RCM characteristic considering motion/force transmissibility”, *Robotica* **43**, 851–867. <https://doi.org/10.1017/S026357472400225X>